Journal of
Materials Chemistry A

ROYAL SOCIETY OF CHEMISTRY

Cu3PS4 Nanoparticle Hole Selective Layer for Efficient Inverted Perovskite Solar Cells

SCHOLARONE™
Manuscripts

Cu₃PS₄ Nanoparticle Hole Selective Layer for Efficient Inverted Perovskite Solar Cells

Xinxing Yin,[§,a,b] Scott A. McClary,[§,c] Zhaoning Song,[a] Dewei Zhao,[a] Brian Graeser,[c] Changlei Wang,[a] Niraj Shrestha,[a] Xiaoming Wang,[a] Cong Chen,[a] Chongwen Li,[a] Kamala K. Subedi,[a] Randy J. Ellingson,[a] Weihua Tang,[b] Rakesh Agrawal,[*,c] and Yanfa Yan[*,a]

[a]Department of Physics and Astronomy, Wright Center for Photovoltaics Innovation and Commercialization, The University of Toledo, Toledo, OH 43606, United States.
[b]Key Laboratory of Soft Chemistry and Functional Materials, Nanjing University of Science and Technology, Nanjing 210094, China
[c] Davidson School of Chemical Engineering, Purdue University, 480 Stadium Mall Drive, West Lafayette, United States

[§] These authors contributed equally to this work.

*Corresponding authors:
Rakesh Agrawal (agrawalr@purdue.edu),
Yanfa Yan (yanfa.yan@utoledo.edu).

Abstract:

Cu$_3$PS$_4$ nanoparticles are used as a new inorganic hole selective layer (HSL) to fabricate efficient perovskite thin-film solar cells in the inverted device configuration. Compared with other HSL materials used in efficient perovskite solar cells, Cu$_3$PS$_4$ has the smallest effective mass for holes. Additionally, Cu$_3$PS$_4$ has a valence band energy level of -5.05 eV, which is suitable for effectively extracting holes generated in perovskite absorbers. These reveal intrinsic properties of Cu$_3$PS$_4$ that make it an excellent HSL material for perovskite solar cells. We further find that Cu$_3$PS$_4$ nanoparticle HSL promotes grain growth of perovskite thin films, which benefits the device performance. Our perovskite solar cells using Cu$_3$PS$_4$ nanoparticle HSL achieve a maximum power conversion efficiency of 18.17% with small hysteresis and a high fill factor of 81.6%, which significantly outperforms the performance of the best control device using poly(3,4-ethylenedioxythiophene)-poly(styrenesulfonate) (PEDOT:PSS) HSL.

1. Introduction

Organic-inorganic metal halide perovskite solar cells (PSCs) have attracted intensive attention in the past few years due to their rapid increase in power conversion efficiencies (PCEs), with a certified record PCE of 23.3% reported recently.[1] The operation of a PSC relies on the use of charge selective layers including the electron selective layer (ESL), which extracts and transfers electrons but blocks holes photogenerated in the perovskite absorber,[2-4] and the hole selective layer (HSL), which extracts and transfers holes but blocks electrons.[5-8] Therefore, besides the material quality and interface passivation of the perovskite absorber, the effectiveness of the ESL and HSL is another key factor determining the PCE of a PSC.[2,9-11] To be charge selective and suppress charge recombination, the ESL and HSL materials should not have high carrier concentrations and must have large bandgaps with suitable energy levels.[12,13] Furthermore, to effectively transfer the extracted charges, small effective masses are highly preferable for the ESL and HSL materials. So far, organic and inorganic ESL and HSL materials have been used.[14-19] In terms of long-term stability of PSCs, inorganic ESL and HSL materials are preferred.[16,20,21] While stable and efficient inorganic ESL materials such as TiO_2,[17,22-24] ZnO,[25,26] and SnO_2 have been used in PSCs,[4,27] current inorganic HSL materials such as NiO_x,[28-30] Cu-delafossites,[31-33] and CuSCN[16,34] underperform the organic counterparts such as poly(bis(4-phenyl)(2,4,6-trimethylphenyl)amine) (PTAA) and 2,2',7,7'-tetrakis(N,N-bis(p-methoxy-phenyl)amino)-9,9'-spirobifluorene (Spiro-OMeTAD).[14,35-37] A major issue of the current inorganic HSL materials is inefficient hole transport, due to their large effective masses for holes.[33,38]

Here, we report a new HSL material, Cu_3PS_4, which has a reasonably small effective mass for holes and a wide-enough bandgap for blocking electrons. Cu_3PS_4 possesses the enargite crystal structure with a symmetry of *Pmn2_1* (**Figure S1**).[39-41] Due to the high symmetry and the d^{10} electronic configuration of Cu, the calculated effective mass for holes is 0.8 m_0, which is much smaller than that of NiO_x (~1 m_0) and Cu delafossites (>3 m_0),[42] enabling high mobility in Cu_3PS_4. Since the valence band maximum (VBM) of Cu_3PS_4 is largely derived from the Cu d^{10} orbital, which has a high energy position, the VBM of Cu_3PS_4 is higher in energy than that of halide perovskite absorbers, leading to efficient hole extraction

from perovskite absorbers. Additionally, Cu_3PS_4 has an indirect bandgap of 2.20 eV, large enough to enable effective electron blocking. Therefore, enargite Cu_3PS_4 is a promising HSL candidate for fabricating efficient PSCs.

In this paper, we evaluate the performance of Cu_3PS_4 nanoparticles (NPs) as an HSL in the inverted device configuration. The use of pre-synthesized Cu_3PS_4 NPs enables us to prepare smooth, compact, and thin HSLs. Our measurements show a VBM level of -5.05 eV and a bandgap of 2.20 eV for Cu_3PS_4 NP HSL, which are suitable for effectively extracting holes generated in perovskite absorbers and blocking electrons, respectively. We further find that Cu_3PS_4 NP HSL promotes grain growth of perovskite thin films, which benefits the device performance. Our PSCs using Cu_3PS_4 NP HSL achieve a maximum PCE of 18.17% with small hysteresis and a high fill factor (FF) of 81.6%, which significantly outperforms the performance of the best control device using PEDOT:PSS HSL, one of the most commonly used organic HSL material that has a similar VBM energy level as Cu_3PS_4 NP HSL. As shown in **Table S1**, Cu_3PS_4 has the smallest effective mass for holes and the best FF compared with other Cu-based HSLs. Our results demonstrate the promise of Cu_3PS_4 NP HSL for fabricating efficient PSCs.

2. Results and discussion

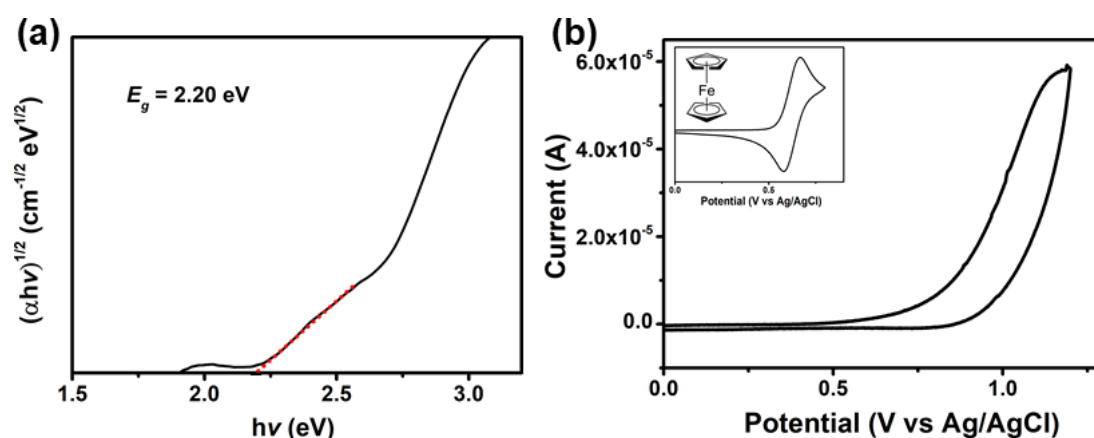**Figure 1.** (a) The T_{auc} plot of a Cu_3PS_4 film coated on a FTO glass substrate. (b) Cyclic voltammograms of Cu_3PS_4 NP films in acetonitrile solution of 0.1 M Bu_4NPF_6. The inset shows CV plot for ferrocene/ferrocenium as reference.

Cu_3PS_4 NPs were synthesized according to Graeser and Agrawal.[40] The structure and phase purity of the NPs ware confirmed via X-ray diffraction (XRD) and Raman spectroscopy

(**Figure S2**). **Figure 1a** shows the T_{auc} plot of a Cu_3PS_4 NP film spin-coated on a fluorine-doped tin oxide (FTO)-coated glass substrate. The thickness of the Cu_3PS_4 NP film is about 20 nm, determined by cross-sectional scanning electron microscopy (SEM) image. The calculated indirect optical bandgap (E_g) is around 2.20 eV. Cyclic voltammetry (CV) was employed to determine the energy level of Cu_3PS_4. Ferrocene/ferrocenium (Fc/Fc$^+$) was adopted as the internal standard, giving a potential of 0.55 V. As shown in **Figure 1b**, a clear oxidation potential of 0.8 V was observed for Cu_3PS_4. The VBM of Cu_3PS_4 was, therefore, calculated to be -5.05 eV. The corresponding conduction band minimum (CBM) was estimated to be -2.85 eV according to the optical bandgap of 2.20 eV.
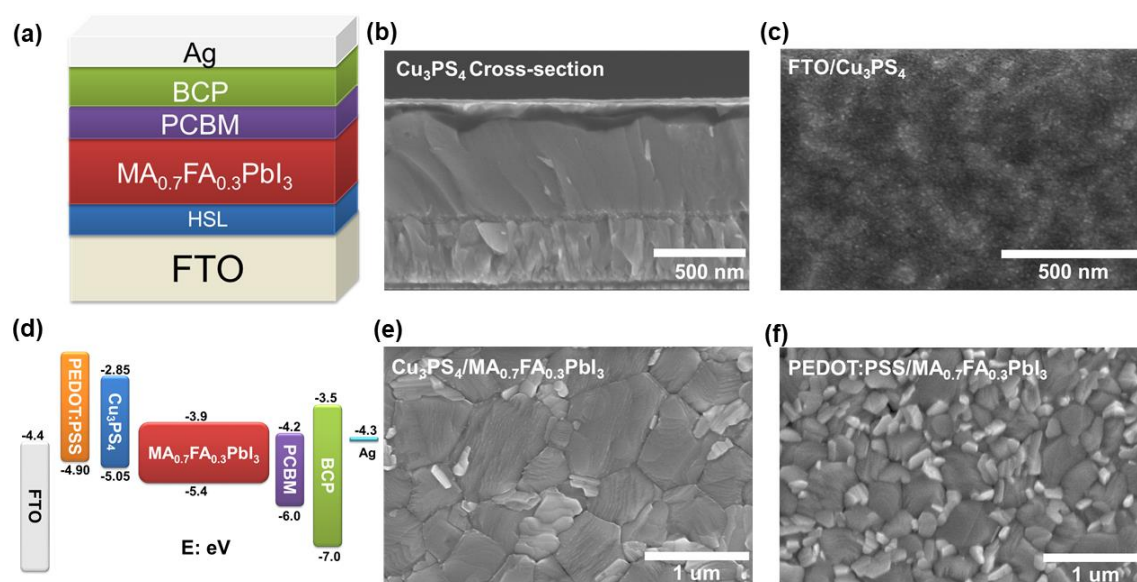

Figure 2. (a) Device structure schematic and (b) cross-sectional SEM image of the p-i-n planar PSC used in this work. (c) Top-view SEM image of a Cu_3PS_4 film deposited on a FTO glass substrate. (d) Energy level diagram of our PSC with PEDOT:PSS or Cu_3PS_4 HSL. Top-view SEM images of perovskite films deposited on (e) Cu_3PS_4 and (f) PEDOT:PSS HSLs.

To evaluate the effectiveness of hole extraction and transport and electron blocking for Cu_3PS_4, we fabricated PSCs with Cu_3PS_4 and PEDOT:PSS HSLs. **Figure 2a** shows the device structure of our PSCs in the inverted (p-i-n) planar structure of FTO/HSL/perovskite/[6,6]-phenyl-C61-butyric acid methyl ester (PCBM)/Bathocuproine (BCP)/Ag, which consists of a Cu_3PS_4 or PEDOT:PSS HSL, a $MA_{0.7}FA_{0.3}PbI_3$ (MA = methylammonium and FA = formamidinium) perovskite absorber, a PCBM/BCP combined

ESL, and a Ag cathode. **Figure 2b** shows a corresponding cross-sectional SEM image of a PSC with a 20 nm Cu_3PS_4 HSL. The compact and uniform morphology of Cu_3PS_4 films, as shown in **Figure 2c**, can be easily obtained through simple spin-coating method. PSC fabrication benefits from a high-quality and pinhole-free HSL layer as seen in our films.[28,43]

The energy band diagram of our PSC is shown in **Figure 2d**. It is seen that the VBM of Cu_3PS_4 is lower than that of PEDOT:PSS (-4.9 eV), which is more favorable for pinning the Fermi level at the perovskite/HSL interface closer to the VBM of the perovskite absorber, consequently benefiting the open-circuit voltage (V_{OC}) of the device. Aside from the more favorable energetic level, we found that the Cu_3PS_4 HSL promotes grain growth of perovskite thin films. As shown in the top-view SEM image (**Figure 2e**), the perovskite film deposited on Cu_3PS_4 HSL shows large grains with the average size of ~750 nm, greatly enlarged from the average size of ~300 nm for the control perovskite films deposited on PEDOT:PSS HSL (**Figure 2f**). Grain boundaries can act as traps and provide paths for ion diffusion and therefore are detrimental for V_{OC} and FF. Perovskite films with large grains are favorable for achieving higher V_{OC} and FF in PSCs.[44-46] The large grains of perovskite films deposited on the Cu_3PS_4 HSL may be attributed to the S component in the Cu_3PS_4 HSL. It has been shown that thiourea additive can promote perovskite grain growth.[47] Moreover, the more hydrophobic surface of Cu_3PS_4 may also facilitate the grain growth (**Figure S3**).[48]

The favorable hole extraction of Cu_3PS_4 HSL is evidenced from the steady-state photoluminescence (PL) (**Figure 3a**) and time-resolved photoluminescence (TRPL) (**Figure 3b**). As shown in **Figure 3a**, the PEDOT:PSS and Cu_3PS_4 HSLs show strong quenching of the PL emission from perovskite film due to the charge transfer at the HSL/perovskite interface. The more pronounced PL quenching observed in the Cu_3PS_4/perovskite than PEDOT:PSS/perovskite is likely the result of better hole transfer. The quenching effect is also clearly seen in the TRPL decays. The measured mean carrier lifetimes for perovskites deposited on bare glass, PEDOT:PSS-coated FTO glass, and Cu_3PS_4-coated FTO glass are 1200, 29, and 16 ns, respectively. Both PL and TRPL results show that the Cu_3PS_4 HSL transfers holes more effectively than PEDOT:PSS HSL, indicating efficient charge extraction at the perovskite/Cu_3PS_4 interface.[5,6]
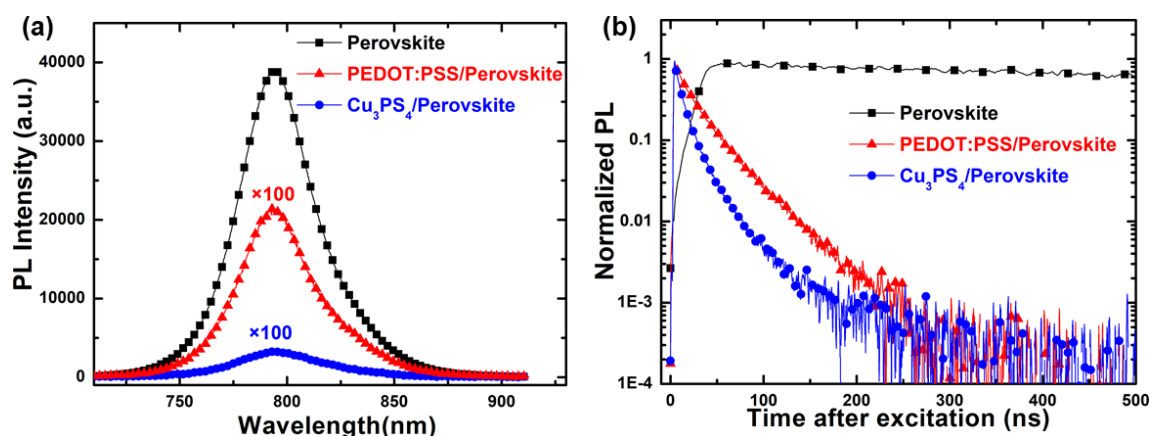
Figure 3. (a) PL spectra and (b) TRPL decays of perovskite film, PEDOT:PSS/perovskite and Cu_3PS_4/perovskite.

We fabricated a large number of PSCs with Cu_3PS_4 HSLs to optimize the device performance. We examined the impact of the thickness of Cu_3PS_4 HSL on the performance of PSCs by varying its thickness from 8 to 33 nm, achieved by controlling both the spin speed and precursor concentration (**Table S2**). As shown in **Figure S4a**, V_{OC} of the devices increased monotonically with increasing thickness of Cu_3PS_4. Limited by the size of Cu_3PS_4 NPs (5-10 nm), Cu_3PS_4 films must be thick enough (e.g., >15 nm) to obtain a continuous and uniform coverage on the FTO electrode. This would prevent shorting paths connecting the perovskite absorber and FTO, which is a prerequisite for high V_{OC} values. However, too thick Cu_3PS_4 films (e.g., >30 nm) introduce significant absorption of photons with wavelengths below 500 nm (see **Figure S5**), resulting in reduced short-circuit current density (J_{SC}) and FF (**Figures S4b, S4c**). The results show that an optimum thickness for Cu_3PS_4 is around 20 nm (**Figure S4d**).
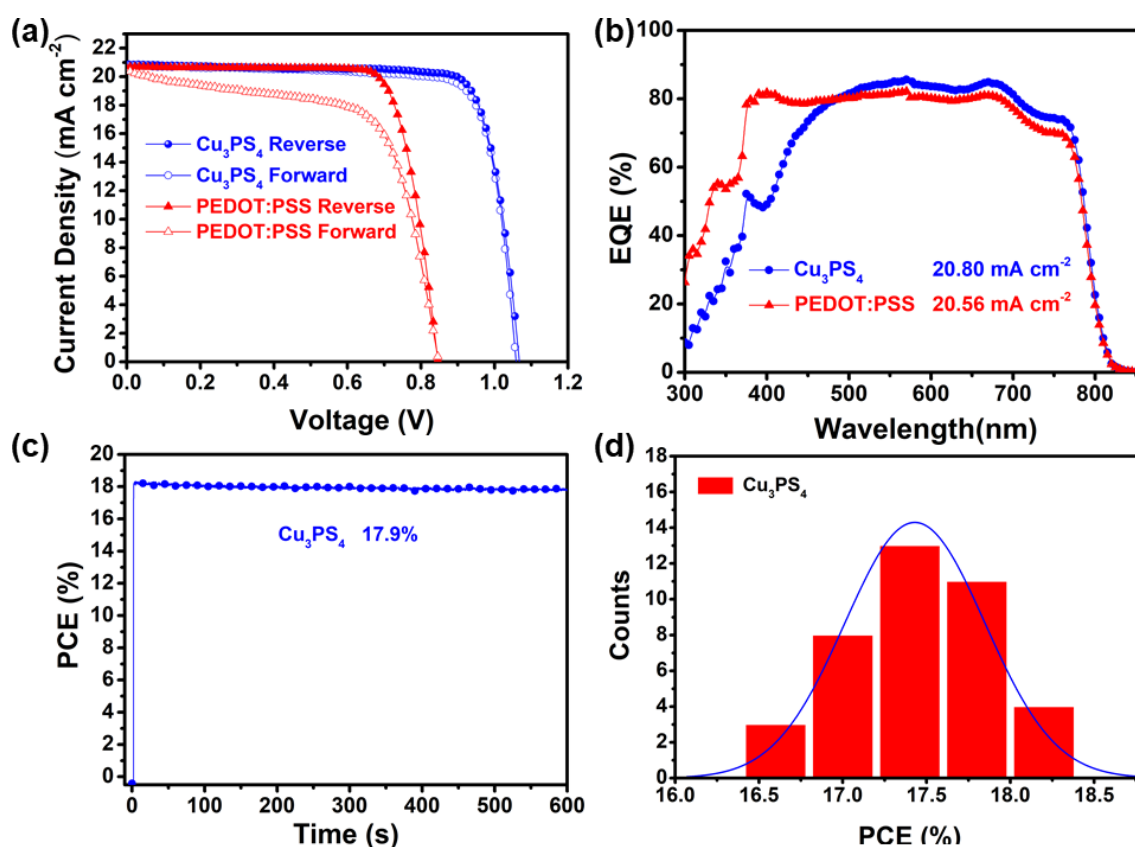
Figure 4. (a) *J-V* curves and (b) EQE spectra of our best-performing PSCs with Cu₃PS₄ or PEDOT:PSS HSL. (c) Steady-state efficiency of the champion PSC with the Cu₃PS₄ HSL. (d) Histogram of PCEs for 40 PSCs using Cu₃PS₄ HSLs.

The PSCs using Cu₃PS₄ HSLs significantly outperform the PSCs using PEDOT:PSS HSLs (**Figure S6**). **Figure 4a** compares the current density-voltage (*J-V*) characteristics of the champion PSCs using Cu₃PS₄ and PEDOT:PSS HSLs, measured under 100 mW cm^{-2} AM1.5G illumination. Our champion device using the Cu₃PS₄ HSL reaches a maximum PCE of 18.17 (17.66)%, with a V_{OC} of 1.069 (1.060) V, a J_{SC} of 20.83 (20.85) mA cm^{-2}, and a FF of 81.6 (79.9)% under reverse (forward) voltage scan. In contrast, the PSC with the PEDOT:PSS HSL exhibits a much inferior PCE of 13.70 (11.30)%, with a V_{OC} of 0.850 (0.840) V, a J_{SC} of 20.67 (20.39) mA cm^{-2}, and a FF of 78.0 (66.0)%. Importantly, the *J-V* hysteresis for the Cu₃PS₄-based device is much lower than that for the PEDOT:PSS-based device. The enhanced PCE of the Cu₃PS₄-based PSC is mainly due to the improvement in both V_{OC} and FF. Compared with PEDOT:PSS, Cu₃PS₄ shows a 0.15 eV deeper VBM level, leading to better energy level match with the perovskite absorber and reduced V_{OC} loss.[18,38] Moreover, the enhancement in V_{OC} is also attributed to the increased grain size shown in

Figure 2e and **2f**, which reduces charge recombination at grain boundaries.[48] The improved FF can be attributed to the enhanced hole extraction by the Cu_3PS_4 layer as discussed before. The EQE-integrated J_{SC}'s over AM1.5G spectrum of PSCs with Cu_3PS_4 or PEDOT:PSS HSL are 20.80 and 20.56 mA cm^{-2} (**Figure 4b**), respectively, which are in agreement with J_{SC}'s obtained from the J-V curves. It is obvious that the Cu_3PS_4-based device exhibits lower spectral responses in the short wavelength region (< 470 nm) due to optical absorption of the Cu_3PS_4 film. However, the higher EQE values in the longer wavelength region (500 to 800 nm), likely due to the enhanced film quality of perovskite absorber, dominate the photocurrent contribution. Additionally, the steady-state power output measurements of PSCs with the Cu_3PS_4 HSL were carried out at a constant bias of 0.930 V for 600 s. Our champion device shows a maximum power point current density of approximately 19.24 mA cm^{-2}, corresponding to a stabilized PCE of ~17.9% (**Figure 4c**). To evaluate the device reproducibility of Cu_3PS_4-based PSCs, we fabricated 40 devices in several different batches. The PCE histogram is shown in **Figure 4d**. The average PCE is 17.43±0.74%, with an average V_{OC} of 1.019±0.058 V, an average J_{SC} of 21.59±0.79 mA cm^{-2}, and an average FF of 79.3±4.4%, measured under the reverse voltage scan.
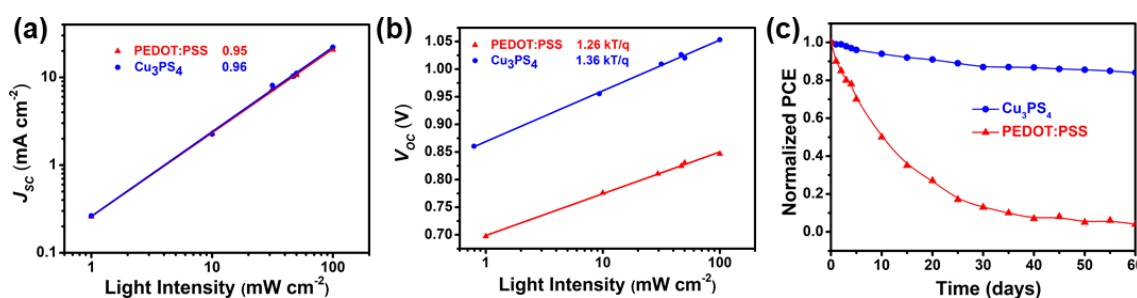

Figure 5. Light-intensity dependence of PSC with Cu_3PS_4 or PEDOT:PSS HSL: (a) J_{sc} versus light intensity and (b) V_{oc} versus light intensity. (c) Stability test of the p-i-n PSCs in ambient air with a humidity of ~50%.

To get a further insight into the charge transport/recombination mechanism in the p-i-n PSCs with Cu_3PS_4 HSL, the power law dependence of J_{SC} on light intensity ($J \propto I^{\alpha}$) was measured under light intensities ranging from 1 to 100 mW cm^{-2} (**Figure 5a**). A linear regression analysis performed on a double logarithmic scale shows α = 0.96 and 0.95 for devices with Cu_3PS_4 and PEDOT:PSS HSLs, indicating the device with the Cu_3PS_4 HSL is

similarly space charge limited as PEDOT:PSS.[6,49] **Figure 5b** shows the relationship of V_{oc} and logarithmic light intensity. The device with Cu_3PS_4 (PEDOT:PSS) HSL has an ideality factor of 1.36 (1.26) kT/q, indicating that trap-assisted Shockley-Read-Hall recombination occurs both in Cu_3PS_4 and PEDOT:PSS devices.[14]

To investigate the device stability of PSCs with Cu_3PS_4 or PEDOT:PSS HSL, we measured the efficiency of unencapsulated PSCs in ambient air at 25 °C and a relative humidity of around 50% (see the PCE decay in **Figure 5c**). For the PEDOT:PSS-based PSC, the PCE dropped almost 50% within only 10 days. This is likely due to the acidic and hygroscopic nature of PEDOT/PSS, which may damage the front electrodes and the adjacent perovskite layers.[12,50] On the contrary, the PSC using the Cu_3PS_4 HSL shows much higher ambient stability, retaining 87% of its initial performance after 60 days. This result is consistent with water contact angle test (**Figure S3b** and **S3c**), Cu_3PS_4 (60°) is much more hydrophobic than PEDOT:PSS (11°). Thus, our inorganic Cu_3PS_4 NPs not only deliver improved device performance, but also enhanced device stability, making it a promising candidate for commercialization of PSCs.

3. Conclusions

In summary, we demonstrate a new inorganic HSL based on Cu_3PS_4 NPs with facile solution processability. A high quality Cu_3PS_4 film is easily obtained through spin coating. Benefiting from the unique surface property of Cu_3PS_4, large perovskite grains with sizes of over 750 nm are acquired. Planar p-i-n PVSCs using Cu_3PS_4 HSLs achieved a maximum PCE of 18.17% with small hysteresis and a steady-state efficiency of 17.90%. Moreover, the Cu_3PS_4-based device without encapsulation retained over 87% of its initial PCE after 60 days in air (25 °C, 50% relative humidity), revealing decent long-term stability. Therefore, Cu_3PS_4 is an excellent candidate as HSLs for further commercialization of the promising PSC technology.

4. Experimental section

4.1. Materials

PEDOT:PSS was purchased from Heraeus (4083). Anhydrous solvents including ethanol,

chlorobenzene, *N,N*-dimethylmethanamide, dimethyl sulfoxide and diethyl ether, as well as copper (II) chloride ($CuCl_2$), phosphorus (V) sulfide (P_2S_5), 1-dodecanethiol (DDT), and oleylamine (OLA) were purchased from Sigma-Aldrich. Hexane and isopropanol (molecular biology grades) were purchased from Fisher. Methylammonium iodide and formamidinium iodide were purchased from Dyesol. Lead iodide and lead thiocyanate were purchased from Alfa. PCBM and BCP were purchased from 1-Material.

4.2. Nanoparticle Synthesis

Cu_3PS_4 nanoparticles were synthesized according to a previous report.[40] Briefly, a flask containing 2 mmol $CuCl_2$, 0.5 mmol P_2S_5, and 4 mL DDT was heated to 250 °C under an inert atmosphere and allowed to react for 1 h. After cooling, the flask's contents were extracted into a centrifuge tube for washing. Three suspension and precipitation cycles using OLA, hexane, and isopropanol were conducted, followed by three cycles using hexane and isopropanol only. The resulting NP pellet was dried under argon flow before use in device experiments.

4.3. Device fabrication

The Florine-doped Tin Oxide (FTO) substrates were cleaned by ultra-sonication in diluted Micro-90 detergent, deionized water, acetone, and isopropanol for 30 min, respectively. A solution of Cu_3PS_4/chlorobenzene (30 mg/mL) was spin-coated on FTO at 4000 rpm for 50 s and annealed at 200 °C for 120 min in N_2. PEDOT:PSS films were coated on cleaned FTO substrates at 4,000 rpm for 50 s and then dried at 175 °C for 30 min in air. The perovskite precursor solution was spin-coated on the HSL layer at 500 rpm for 3 s and at 4000 rpm for 60 s using diethyl ether as anti-solvent.[5,6,8] After spin coating, the perovskite film was annealed at 100 °C for 5 min. PCBM (20 mg/mL in chlorobenzene) was then deposited on the perovskite film at 2000 rpm for 30 s and annealed at 90 °C for 10 min. BCP (0.5 mg/mL in ethanol) was spin-coated on the PCBM film at 4000 rpm for 30 s. A layer of 75 nm silver (Ag) was then deposited on the top using thermal evaporation. The working area of the devices was 0.08 cm^2 as defined by a shadow mask during the Ag evaporation.

4.4. Material, film and device characterization

Grazing incidence X-ray diffraction (XRD) data were taken using a Rigaku Smartlab diffractometer (Cu Kα source) in parallel beam geometry with an incident angle of 0.5°. Raman spectra were collected using a 633 nm He:Ne laser coupled with a Horiba/Jovin-Yvon LabRAM HR800 confocal microscope at a magnification of 100x. The electrochemical cyclic voltammetry (CV) was conducted on an electrochemical workstation with Pt plate as working electrode, Pt slice as counter electrode, and Ag/AgCl electrode as reference electrode in tetrabutylammonium hexafluorophosphate (Bu_4NPF_6, 0.1 M) acetonitrile solutions at a scan rate of 50 mV s^{-1}. Ferrocene/ferrocenium (Fc/Fc^+) was used as the internal standard (the energy level of Fc/Fc^+ is -4.8 eV under vacuum), and the formal potential of Fc/Fc^+ was measured as 0.55 V vs. Ag/AgCl electrode. The HOMO energy level was determined from the onset oxidation (E_{onset}^{ox}) as HOMO = $-4.25 - E_{onset}^{ox}$ (eV); while the LUMO energy level was calculated with HOMO and optical bandgap (E_g) by the formula as: LUMO = HOMO + E_g(eV).

Film characterization: High resolution field emission top-view and cross-sectional SEM images of all films and completed devices were taken with a Hitachi S-4800 SEM. All layer thicknesses were determined using a Dektak surface profiler and cross-sectional SEM images. TRPL measurements were conducted similarly as described in our earlier works.[49,51]

Device characterization: *J-V* curves were measured in air under 100 mW/cm^2 AM1.5G solar irradiation (PV Measurements Inc.) with a Keithley 2400 Source Meter. The incident light was controlled by a shutter. The light intensity for *J-V* measurements was calibrated by a standard Si solar cell and our perovskite solar cells certified by Newport.[48] The steady-state efficiencies were obtained by tracking the maximum output power point. EQE spectra were performed on a QE system (PV Measurements Inc., model IVQE8-C QE system without bias voltage) using 100 Hz chopped monochromatic light ranging from 300 to 850 nm under near-dark test conditions. All characterizations and measurements were performed in the ambient.

Acknowledgements

Statement of Data Access

Data associated with this manuscript can be found at the project's website:

https://datacenterhub.org/groups/dmref1534691.

References

1.   NREL, Best Research Cell Effciencies (accessed: July 2018), https://www.nrel.gov/pv/assets/images/efficiency-chart-20180716.jpg.
2.   L. Meng, J. You, T.-F. Guo and Y. Yang, *Acc. Chem. Res.*, 2016, **49**, 155-165.
3.   C. Wang, C. Xiao, Y. Yu, D. Zhao, R. A. Awni, C. R. Grice, K. Ghimire, D. Constantinou, W. Liao, A. J. Cimaroli, P. Liu, J. Chen, N. J. Podraza, C.-S. Jiang, M. M. Al-Jassim, X. Zhao and Y. Yan, *Adv. Energy Mater.*, 2017, **7**, 1700414.
4.   G. Yang, C. Chen, F. Yao, Z. Chen, Q. Zhang, X. Zheng, J. Ma, H. Lei, P. Qin, L. Xiong, W. Ke, G. Li, Y. Yan and G. Fang, *Adv. Mater.*, 2018, **30**, 1706023.
5.   X. Yin, L. Guan, J. Yu, D. Zhao, C. Wang, N. Shrestha, Y. Han, Q. An, J. Zhou, B. Zhou, Y. Yu, C. R. Grice, R. A. Awni, F. Zhang, J. Wang, R. J. Ellingson, Y. Yan and W. Tang, *Nano Energy*, 2017, **40**, 163-169.
6.   X. Yin, C. Wang, D. Zhao, N. Shrestha, C. R. Grice, L. Guan, Z. Song, C. Chen, C. Li, G. Chi, B. Zhou, J. Yu, Z. Zhang, R. J. Ellingson, J. Zhou, Y. Yan and W. Tang, *Nano Energy*, 2018, **51**, 680-687.
7.   Y. Sun, C. Wang, D. Zhao, J. Yu, X. Yin, C. R. Grice, R. A. Awni, N. Shrestha, Y. Yu, L. Guan, R. J. Ellingson, W. Tang and Y. Yan, *Solar RRL*, 2018, **2**, 1700175.
8.   L. Guan, X. Yin, D. Zhao, C. Wang, Q. An, J. Yu, N. Shrestha, C. Grice, R. Awni, Y. Yu, Z. Song, J. Zhou, W. Meng, F. Zhang, R. Ellingson, J. Wang, W. Tang and Y. Yan, *J. Mater. Chem. A*, 2017, **5**, 23319-23327.
9.   Y. Bai, X. Meng and S. Yang, *Adv. Energy Mater.*, 2018, **8**, 1701883.

10.	A. Fakharuddin, L. Schmidt-Mende, G. Garcia-Belmonte, R. Jose and I. Mora-Sero, *Adv. Energy Mater.*, 2017, **7**, 1700623.

11.	M. L. Petrus, J. Schlipf, C. Li, T. P. Gujar, N. Giesbrecht, P. Müller-Buschbaum, M. Thelakkat, T. Bein, S. Hüttner and P. Docampo, *Adv. Energy Mater.*, 2017, **7**, 1700264.

12.	L. Calió, S. Kazim, M. Grätzel and S. Ahmad, *Angew. Chem., Int. Ed.*, 2016, **55**, 14522-14545.

13.	J.-P. Correa-Baena, A. Abate, M. Saliba, W. Tress, T. Jesper Jacobsson, M. Gratzel and A. Hagfeldt, *Energy Environ. Sci.*, 2017, **10**, 710-727.

14.	N. J. Jeon, H. Na, E. H. Jung, T.-Y. Yang, Y. G. Lee, G. Kim, H.-W. Shin, S. Il Seok, J. Lee and J. Seo, *Nat. Energy*, 2018, **3**, 682-689.

15.	Y. Hou, X. Du, S. Scheiner, D. P. McMeekin, Z. Wang, N. Li, M. S. Killian, H. Chen, M. Richter and I. Levchuk, *Science*, 2017, **358**, 1192-1197.

16.	N. Arora, M. I. Dar, A. Hinderhofer, N. Pellet, F. Schreiber, S. M. Zakeeruddin and M. Grätzel, *Science*, 2017, **358**, 768-771.

17.	H. Tan, A. Jain, O. Voznyy, X. Lan, F. P. García de Arquer, J. Z. Fan, R. Quintero-Bermudez, M. Yuan, B. Zhang, Y. Zhao, F. Fan, P. Li, L. N. Quan, Y. Zhao, Z.-H. Lu, Z. Yang, S. Hoogland and E. H. Sargent, *Science*, 2017, **355**, 722-726.

18.	D. Zhao, C. Chen, C. Wang, M. M. Junda, Z. Song, C. R. Grice, Y. Yu, C. Li, B. Subedi, N. J. Podraza, X. Zhao, G. Fang, R.-G. Xiong, K. Zhu and Y. Yan, *Nat. Energy*, 2018, **3**, 1093-1100.

19.	R. Xue, M. Zhang, G. Xu, J. Zhang, W. Chen, H. Chen, M. Yang, C. Cui, Y. Li and Y. Li, *J. Mater. Chem. A*, 2018, **6**, 404-413.

20.	Z. H. Bakr, Q. Wali, A. Fakharuddin, L. Schmidt-Mende, T. M. Brown and R. Jose, *Nano Energy*, 2017, **34**, 271-305.

21.	J. Sun, J. Lu, B. Li, L. Jiang, A. S. R. Chesman, A. D. Scully, T. R. Gengenbach, Y.-B. Cheng and J. J. Jasieniak, *Nano Energy*, 2018, **49**, 163-171.

22.	M. M. Byranvand, T. Kim, S. Song, G. Kang, S. U. Ryu and T. Park, *Adv. Energy Mater.*, 2018, **8**, 1702235.

23.	T.-P. Chen, C.-W. Lin, S.-S. Li, Y.-H. Tsai, C.-Y. Wen, W. J. Lin, F.-M. Hsiao, Y.-P. Chiu, K. Tsukagoshi, M. Osada, T. Sasaki and C.-W. Chen, *Adv. Energy Mater.*, 2018, **8**, 1701722.

24.	M. M. Tavakoli, P. Yadav, R. Tavakoli and J. Kong, *Adv. Energy Mater.*, 2018, **8**, 1800794.

25.	P. Zhang, J. Wu, T. Zhang, Y. Wang, D. Liu, H. Chen, L. Ji, C. Liu, W. Ahmad, Z. D. Chen and S. Li, *Adv. Mater.*, 2018, **30**, 1703737.

26.	J. Cao, B. Wu, R. Chen, Y. Wu, Y. Hui, B.-W. Mao and N. Zheng, *Adv. Mater.*, 2018, **30**, 1705596.

27.	L. Xiong, Y. Guo, J. Wen, H. Liu, G. Yang, P. Qin and G. Fang, *Adv. Funct. Mater.*, 2018, **28**, 1802757.

28.	Z. Y. Liu, J. J. Chang, Z. H. Lin, L. Zhou, Z. Yang, D. Z. Chen, C. F. Zhang, S. Z. Liu and Y. Hao, *Adv. Energy Mater.*, 2018, **8**, 1703432.

29.	W. Chen, Y. Wu, J. Fan, A. B. Djurišić, F. Liu, H. W. Tam, A. Ng, C. Surya, W. K. Chan, D. Wang and Z. B. He, *Adv. Energy Mater.*, 2018, **8**, 1703519.

30. W. Nie, H. Tsai, J.-C. Blancon, F. Liu, C. C. Stoumpos, B. Traore, M. Kepenekian, O. Durand, C. Katan, S. Tretiak, J. Crochet, P. M. Ajayan, M. Kanatzidis, J. Even and A. D. Mohite, *Adv. Mater.*, 2018, **30**, 1703879.

31. H. Zhang, H. Wang, W. Chen and A. K. Y. Jen, *Adv. Mater.*, 2017, **29**, 1604984.

32. H. Zhang, H. Wang, H. Zhu, C.-C. Chueh, W. Chen, S. Yang and A. K. Y. Jen, *Adv. Energy Mater.*, 2018, **8**, 1702762.

33. W. A. Dunlap-Shohl, T. B. Daunis, X. Wang, J. Wang, B. Zhang, D. Barrera, Y. Yan, J. P. Hsu and D. B. Mitzi, *J. Mater. Chem. A*, 2018, **6**, 469-477.

34. N. Wijeyasinghe, A. Regoutz, F. Eisner, T. Du, L. Tsetseris, Y.-H. Lin, H. Faber, P. Pattanasattayavong, J. Li, F. Yan, M. A. McLachlan, D. J. Payne, M. Heeney and T. D. Anthopoulos, *Adv. Funct. Mater.*, 2017, **27**, 1701818.

35. D. Luo, W. Yang, Z. Wang, A. Sadhanala, Q. Hu, R. Su, R. Shivanna, G. F. Trindade, J. F. Watts, Z. Xu, T. Liu, K. Chen, F. Ye, P. Wu, L. Zhao, J. Wu, Y. Tu, Y. Zhang, X. Yang, W. Zhang, R. H. Friend, Q. Gong, H. J. Snaith and R. Zhu, *Science*, 2018, **360**, 1442-1446.

36. S. S. Shin, E. J. Yeom, W. S. Yang, S. Hur, M. G. Kim, J. Im, J. Seo, J. H. Noh and S. I. Seok, *Science*, 2017, **356**, 167-171.

37. W. S. Yang, B.-W. Park, E. H. Jung, N. J. Jeon, Y. C. Kim, D. U. Lee, S. S. Shin, J. Seo, E. K. Kim, J. H. Noh and S. I. Seok, *Science*, 2017, **356**, 1376-1379.

38. G. Hautier, A. Miglio, G. Ceder, G.-M. Rignanese and X. Gonze, *Nat. Commun.*, 2013, **4**, 2292.

39. E. J. Sheets, Purdue University, 2015.

40. B. Graeser and R. Agrawal, *RSC Adv.*, 2018, **8**, 34094-34101.

41. T. Shi, W.-J. Yin, M. Al-Jassim and Y. Yan, *Appl. Phys. Lett.*, 2013, **103**, 152105.

42. K. Yim, Y. Youn, M. Lee, D. Yoo, J. Lee, S. H. Cho and S. Han, *npj Comput. Mater.*, 2018, **4**, 17.

43. J. Fei, C. W. C. H., L. Xinchen, Z. Di and C. Jiaqi, *Adv. Mater.*, 2015, **27**, 2930-2937.

44. J. Huang, Y. Yuan, Y. Shao and Y. Yan, *Nat. Rev. Mater.*, 2017, **2**, 17042.

45. W. Nie, H. Tsai, R. Asadpour, J.-C. Blancon, A. J. Neukirch, G. Gupta, J. J. Crochet, M. Chhowalla, S. Tretiak, M. A. Alam, H.-L. Wang and A. D. Mohite, *Science*, 2015, **347**, 522-525.

46. C. Wang, Z. Song, Y. Yu, D. Zhao, R. A. Awni, C. R. Grice, N. Shrestha, R. J. Ellingson, X. Zhao and Y. Yan, *Sustainable Energy Fuels*, 2018, **2**, 2435-2441.

47. J.-W. Lee, H.-S. Kim and N.-G. Park, *Acc. Chem. Res.*, 2016, **49**, 311-319.

48. C. Bi, Q. Wang, Y. Shao, Y. Yuan, Z. Xiao and J. Huang, *Nat. Commun.*, 2015, **6**, 7747.

49. D. Zhao, Y. Yu, C. Wang, W. Liao, N. Shrestha, C. R. Grice, A. J. Cimaroli, L. Guan, R. J. Ellingson, K. Zhu, X. Zhao, R.-G. Xiong and Y. Yan, *Nat. Energy*, 2017, **2**, 17018.

50. M. P. de Jong, L. J. van IJzendoorn and M. J. A. de Voigt, *Appl. Phys. Lett.*, 2000, **77**, 2255-2257.

51. W. Liao, D. Zhao, Y. Yu, N. Shrestha, K. Ghimire, C. R. Grice, C. Wang, Y. Xiao, A. J. Cimaroli, R. J. Ellingson, N. J. Podraza, K. Zhu, R.-G. Xiong and Y. Yan, *J. Am. Chem. Soc.*, 2016, **138**, 12360-12363.